

Enhancing Stability, Magnetic Anisotropy, and Coercivity of τ -L1₀ MnAl: Machine Learning, *Ab Initio*, and Micromagnetic Modeling

Churna Bhandari,^{1,*} Gavin N. Nop,^{1,2} T. Lograsso,¹ and Durga Paudyal^{1,3,†}

¹The Ames National Laboratory, U.S. Department of Energy, Iowa State University, Ames, Iowa 50011, USA

²Department of Mathematics, Iowa State University, Ames, Iowa 50011, USA

³Department of Electrical and Computer Engineering, Iowa State University, Ames, Iowa 50011, USA

The binary manganese aluminium (MnAl) alloy with L1₀ crystal structure is a promising rare earth element-free permanent magnetic material because of its exceptional magnetic properties. However, experimentally synthesizing it in a stable bulk form is extremely challenging. Here, an alternative method of stabilizing the material is proposed and theoretically verified by partially substituting Mn and Al sites with Fe and Ni and identifying its enhanced phase stability, magnetic anisotropy, and coercivity from density functional theory (DFT), machine learning (ML) crystal graph convolution neural network (CGCNN), and micro-magnetic modeling. When considering a fixed (50%)-Ni, the magnetic anisotropy increases with the increasing Fe content but decreases the formation energy. The calculated formation energies, elastic constants, and phonon frequencies demonstrate that all the binary and quaternary compositions are stable. Most importantly, the magnetic moment and magnetic anisotropy constants in 50%-Fe substituted composition (equiatomic phase) increase significantly compared to the MnAl. The predicted coercivity of the equiatomic phase is larger than the parent compound calculated by combining DFT computed parameters with micro-magnetic simulations.

I. INTRODUCTION

Since the early 1900s experiments on binary alloys conducted by Hindiricks[1] and by Ishiwara [2], there has been an ongoing pursuit to harness the critical element-free ferromagnetic equiatomic MnAl with τ -L1₀ phase for permanent magnet applications[3–6]. The τ - phase with L1₀ type tetragonal crystal symmetry transforms from the non-magnetic hexagonal ϵ -phase[7] under specific cooling conditions within a narrow range of (\sim 51 – 58%) Mn-stoichiometric conditions[3, 4]. Although it is metastable, it possesses high magnetic moment [8], magnetic anisotropy[9, 10], Curie temperature[3, 11] ($T_C = 380^\circ\text{C}$ or 653.15 K), and maximum energy product, $BH_{max} = 12 \text{ KJ/m}^3$ (14 MGOe)[12]. These modest magnetic properties enable it to be a promising gap magnet that fulfills the performance gap between low-performing ferrites [13–15] and high-performing rare-earth permanent magnets[12, 16–18]. However, synthesizing it in bulk form is challenging, except the specific forms such as ribbons[19] and thin films[10, 20, 21]. Introducing dopants[4, 9, 22], such as carbon, can improve its structural, mechanical[9], and thermal[23] stabilities, resulting in the formation of a ternary MnAlC. Nonetheless, this approach leads to a decrease in T_C [4, 11, 24, 25] and anisotropy field[9], including an increase in manufacturing cost due to the hot extrusion process[26].

The L1₀ crystal structure is commonly found in a family of ferromagnetic materials, FePd, FePt, and CoPt binaries. This structure forms due to the first-order transition from cubic (A₁) structure at low temperatures[5, 6]

by a nucleation and growth process. The conventional L1₀ crystal structure consists of ABC₂ arrangements[27] (4 basis atoms per unit cell, space group 123 $P4/mmm$, the Pearson symbol tP4 [28]), where three sublattices A, B, and C occupy $1a(0, 0, 0)$, $1c(1/2, 1/2, 0)$, and $2e(1/2, 0, 1/2)$ and $(0, 1/2, 1/2)$ Wyckoff sites, respectively. As the CuAu(I) L1₀-type structure has only two types of basis atoms, its crystal structure can be described either by a four-atom base-centered tetragonal cell (tP4) or a two-atom tetragonal unit cell (Pearson symbol tP2 [28]). The tetragonal unit cell with lattice constants ($c' = c$ and $a' = a/\sqrt{2}$, where c and a are the lattice vectors of tP4 unit cell) is composed of two distinct basis atoms occupying $1a(0, 0, 0)$ and $1d(1/2, 1/2, 1/2)$ Wyckoff positions.

In general, MnAl exhibits a stable antiferromagnetic phase when it has a high Mn content $\text{Mn} > 50\%$ [29]. However, achieving the equiatomic MnAl τ -phase is not straightforward as excess Mn atoms tend to occupy Al sites, easily decomposing into equilibrium phases, including γ_2 -Mn₅Al₈ (space group $R3m$) and β -Mn (space group $P4_{132}$)[30]. When the Mn content decreases gradually, it transitions into a ferromagnetic state exhibiting a strong Mn-dependent Curie temperature[31]. MnAl forms a ferromagnetic metastable τ - phase, a nominal L1₀ CuAu(I)-type tetragonal structure, through the cooling of the high-temperature ϵ -phase, with a space group of $P6_3/mmc$ [4] or through annealing[32]. In a separate experiment, Klemmer *et al.* reported that the τ phase emerges via shear or displacive transformation[6]. However, it is prone to issues such as large grain size, antiphase boundaries, and twin-like defects[33, 34], which negatively affect its magnetic properties.

To improve the stability and magnetic properties of MnAl alloys, various elements such as Ti, Cu, Ni, Co, B[35], Fe[30], Co[36], Ni[37], Cu[38], Zn[39], and rare

* Corresponding Author: cbb@ameslab.gov

† Current Address: Department of Physics and Astronomy, University of Iowa, Iowa City, Iowa 52242, USA

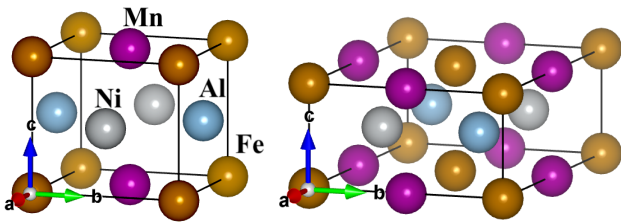


FIG. 1. The simulated crystal structures of site substituted MnAl i.e., FeMnAlNi ABC₂ L₁₀ type distorted tetragonal (*Pmmm* space group no. 47) *left* and monoclinic crystal with space group no. 10 derived from the tetragonal τ -L₁₀ crystal of metastable MnAl with space group no. 123 *P4/mmm* *right*.

earth elements (Pr and Dy)[40] have been substituted into the MnAl alloy. In a study by Saravanan *et al.*[38], Cu-substituted MnAl exhibited exceptionally high coercivity (H_c). C and Zn have been shown to enhance the stability, coercivity, and saturation magnetization of the τ -phase[11, 39], while Fe alone has been predicted to enhance the magnetic anisotropy[30]. However, although C stabilizes the τ phase, it does not prevent the formation of equilibrium phases during annealing[31]. In this work, an alternative approach is proposed to enhance stability and magnetic properties by introducing Fe and Ni simultaneously.

In this paper, a first-principles study is presented for the stability, electronic properties, magnetic properties, and H_c along with micromagnetic modeling of pristine and site substituted MnAl alloys. The phase stabilities are investigated by calculating formation energy, mechanical properties, and phonon dispersions. The site substituted MnAl alloys are stable compared to other unary and potential binary phases. The formation energy and saturation magnetization density are explored by machine learning (ML) study on density functional theory (DFT) calculated magnetic materials. The calculations of elastic properties confirm the mechanical stability of all compositions. The absence of soft-mode frequencies in the phonon dispersion indicates their dynamic stability. The introduction of dopants leads to changes in the electronic structure, affecting the magnetic moments and anisotropy. In particular, improvements are predicted in the magnetic anisotropy and coercivity for the equiatomic phase consisting of equal amounts of Fe, Mn, Al, and Ni obtained by simultaneous doping with Fe and Ni.

II. CRYSTAL STRUCTURE AND METHODOLOGY

The Vienna simulation package (VASP) was used to solve Kohn-Sham eigenvalue equations with generalized gradient approximation Perdew-Burke-Ernzerhof (PBE) functional[41, 42] within the projector augmented wave method (PAW)[43, 44]. The structure was relaxed using

TABLE I. Optimized lattice parameters of pristine and Fe/Ni-substituted MnAl in units of \AA and comparison with available experiments.

System	a	b	c
MnAl	2.76	2.76	3.46
Expt.	2.77[3, 46]	2.77	3.57[3], 3.59[46]
	2.75[47]	2.75	3.56[47]
	2.769[25]	2.769	3.618[25]
FeMnAlNi ^a	3.37	3.79	3.81
Fe _{0.5} Mn _{1.5} AlNi	7.18	5.18	2.69
Mn ₂ AlNi	7.12	5.24	2.73

a plane-wave energy cutoff of 520 eV and a $9 \times 9 \times 7$ \mathbf{k} -mesh for Brillouin zone integration in MnAl with similar \mathbf{k} -meshes for site substituted-compositions proportional to their supercell lattice constants, including for distorted tetragonal L₁₀ structure. To obtain the magnetocrystalline anisotropy (MCA), fully self-consistent relativistic calculations were performed, including the spin-orbit interaction as implemented in the VASP [45]. To achieve the convergence of the magnetic anisotropy energy, several calculations were performed varying \mathbf{k} -mesh up to $14 \times 14 \times 13$ for MnAl, $10 \times 10 \times 10$ for FeMnAlNi, and $7 \times 10 \times 19$ for other partially site substituted systems commensurate with lattice constants.

For the site substituted-compositions, the two lowest total energy structures were used among the considered crystal structures (i) a 4 atom standard L₁₀ tP4 unit cell for FeMnAlNi as shown in Fig. 1 *left* and (ii) an 8 atom new supercell Fig. 1 *right*. In the L₁₀ unit cell, one Mn was replaced by Fe and one Al by one Ni, and the resulting structure has the same proportion of four elements, which is considered as an equiatomic phase. This crystal structure with space group no. 47 *Pmmm* is spanned by Fe, Mn, Al, and Ni atoms occupying $1a$, $1f$, $1d$, and $1g$ Wyckoff sites. For structure (ii), a $2 \times 2 \times 1$ supercell was built from τ -L₁₀-type (tP2 unit cell) structure by partially replacing Mn and Al with Fe and Ni. For FeMnAlNi, a primitive cell with space group no. 10 from the supercell was built, which is utilized in the calculations. The crystal structures are spanned by the four inequivalent sublattices Fe, Mn, Al, and Ni at $1a$, $1g$, $1e$, and $1f$ Wyckoff positions in FeMnAlNi. However, as discussed later in Section III A, it is noted that the total energy is higher for this structure. For FeMnAlNi, only the L₁₀ tP4 type unit cell (i) results are shown. The unit cell (ii) is used for the partially (25%) Fe-and 50% Ni-substituted composition (Fe_{0.5}Mn_{1.5}AlNi). The crystal structure of Fe_{0.5}Mn_{1.5}AlNi is spanned by the four-six inequivalent sublattices Fe at $1a$, Mn₁ at $1g$, Mn₂ at $1c$, Mn₃ at $1d$, Al at $2n$, and Ni at $2n$ Wyckoff positions. The same supercell is used for the Ni-only substituted case, Mn₂AlNi, but it has a different space group, no. 65 occupied by three sublattices, Mn, Al, and Ni, at $4a$, $2c$, and $2d$ Wyckoff positions.

Optimized lattice constants are presented in Table I.

For MnAl, the PBE functional produces in-plane lattice constants very close to the experiment, although it underestimates the out-of-plane lattice constant (c). The out-of-plane lattice constant reduces by $\sim 3\%$ contrary to the GGA functional, which generally yields 1 – 2% larger for other materials. However, it is noted that the experimental lattice constants are obtained in different measurement conditions. For instance, Kinemuchi *et al.* measured at high pressure (> 5 GPa) [46]. Koch *et al.*, on the other hand, found slightly different values under cooling at an average rate of $30^\circ/\text{sec}$ at higher temperature[3]. The lattice constants decrease with increasing Fe, as expected, because its atomic size is smaller than Mn.

The FM state with all atoms spins except Al is parallel and has a lower energy by about 0.33 eV than the AFM structure for FeMnAlNi. Other compositions are also FM. In Mn_2AlNi , FM-aligned Mn-spins have lower energy by 19 meV/atom relative to the AFM compared to Fe-doped compositions. These results suggest that as soon as Ni is introduced, the L1_0 - τ state continues to be the FM. It is noted that Mn_2AlNi has heusler[48] type face-centered cubic crystal structure (space group no. 216), which is an AFM.

III. PHASE STABILITY

A. Formation energy from DFT

The formation energy is examined relative to i) unaries and ii) binaries MnAl, FeNi, AlNi, and MnFe. The formation energy of $\text{Fe}_2\text{Mn}_2\text{Al}_2\text{Ni}_2$ (FeMnAlNi) with respect to the unaries is determined using the equation:

$$E_f[\text{Fe}_2\text{Mn}_2\text{Al}_2\text{Ni}_2] = E[\text{Fe}_2\text{Mn}_2\text{Al}_2\text{Ni}_2] - \sum_i n_i E_i, \quad (1)$$

where E_f represents the formation energy, $E[\text{Fe}_2\text{Mn}_2\text{Al}_2\text{Ni}_2]$ and E_i denote the energies of $\text{Fe}_2\text{Mn}_2\text{Al}_2\text{Ni}_2$ and the i^{th} element, and n_i represents the number of i^{th} -element present in the unit cell. With respect to the binaries, the formation energy is calculated as:

$$E_f[\text{Fe}_2\text{Mn}_2\text{Al}_2\text{Ni}_2] = E[\text{Fe}_2\text{Mn}_2\text{Al}_2\text{Ni}_2] - 2E[\text{MnAl}] - 2E[\text{FeNi}], \quad (2)$$

where $E[\text{MnAl}]$ and $E[\text{FeNi}]$ correspond to the energies of MnAl and FeNi, respectively.

In both cases, the computed formation energies for all compositions are negative, as shown in Figure 2. As discussed earlier, 50%-Fe- and Ni-doped alloys can form two probable structures. However, the total energy of tetragonal FeMnAlNi is lower by 0.33 eV/f.u. than in a monoclinic structure. In fact, the monoclinic structure has positive formation energy (9 meV/atom) with respect to

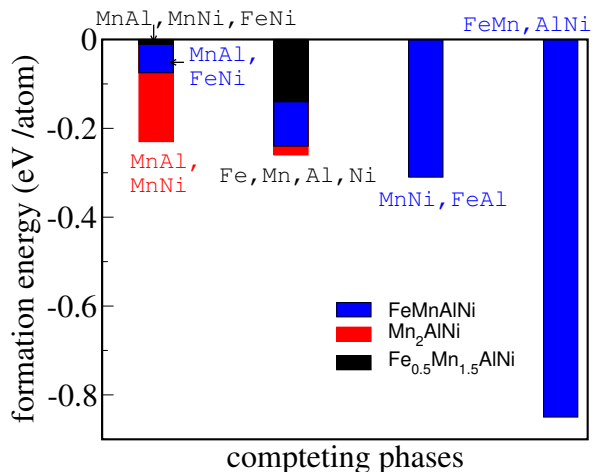


FIG. 2. Formation energy of Fe/Ni-doped MnAl alloy as a function of various binaries and unaries. The formation energy is negative in all phases. The 50%Fe and 50%Ni-doped composition has distorted L1_0 type structure.

MnAl and FeNi binaries, suggesting it is an energetically unstable structure. The Mn_2AlNi exhibits a similar negative formation energy. This is the heusler-type face-centered cubic crystal structure [48, 49], which is antiferromagnetic (AFM) and therefore is not important for permanent magnet applications.

B. Mechanical stability

The energy strain relation was employed to compute the mechanical properties, which, in Voigt notation, reads

$$E = \frac{V_0}{2} \sum_{i=1}^6 \sum_{j=1}^6 C_{ij} \epsilon_i \epsilon_j, \quad (3)$$

where V_0 is the volume of unit cell, C_{ij} are the elastic constants, and ϵ_i are components of strain tensor. The calculated elastic stiffness matrix [Appendix Eq. (A1)] for MnAl is definite positive, has all positive eigenvalues, and its elements satisfy the mechanical stability criteria for tetragonal structure[50]

$$C_{11} > |C_{12}|, \quad 2C_{13}^2 < C_{33}(C_{11} + C_{12}), \quad \text{and} \quad C_{44} > 0.$$

Here, the elastic stiffness matrices are definite positive and satisfy the criteria for mechanical stability. For the distorted tetragonal structure, mechanical criteria[51] $C_{11} > 0$, $C_{11} * C_{22} > C_{12}^2$, $C_{11} * C_{22} * C_{33} + 2C_{12} * C_{13} * C_{23} - C_{11} * C_{23}^2 - C_{22} * C_{13}^2 - C_{33} * C_{12}^2 > 0$, $C_{44} > 0$, $C_{55} > 0$, and $C_{66} > 0$ are satisfied.

The bulk modulus is larger in the substituted alloys, suggesting a slight increase in stiffness, while the shear modulus is the opposite with respect to pristine composition. Overall, both compositions show similar elastic

TABLE II. Bulk Modulus (K), Shear Modulus (G), Young's Modulus (E), Poisson's Ratio (ν) in GPa and Poisson and bulk to shear modulus ratio of MnAl in Voigt notations.

parameters	MnAl	FeMnAlNi	Fe _{0.5} Mn _{1.5} AlNi
K	132.62	139.60	128.75
G	98.34	80.08	80.68
E	236.55	201.68	200.22
ν	0.20	0.26	0.24
K/G	1.35	1.74	1.60

properties. Similarly, Fe_{0.5}Mn_{1.5}AlNi and Mn₂AlNi are found mechanically stable as the elastic constants presented in A3 and A4 satisfy the stability criteria given in Ref. ([51]). Fe lowers the stiffness at 25% and increases slightly at 50% (II).

C. Phonon dynamics

The frozen-phonon method[52] was used to compute the phonon frequencies. The calculations were performed with the phonopy package[53], building $4 \times 4 \times 4$ supercells for pristine materials and $2 \times 2 \times 4$ supercells for doped compounds. For FeMnAlNi, distorted tetragonal structure, a $3 \times 3 \times 3$ supercell was used. The dynamical matrix was computed using a well-converged \mathbf{k} -point mesh, which was further diagonalized to produce phonon frequencies with phonopy. Figure 3 shows the phonon dispersion along the high symmetry \mathbf{k} -points for (a) pristine and (b) - (d) doped-MnAl, obtained through GGA calculations.

Figure 3 (b) shows the phonon dispersion for distorted tetragonal FeMnAlNi. The absence of imaginary phonon frequencies in doped and pristine compositions ensure their dynamical stability. Analyzing the atom-projected phonon density of states for MnAl, it becomes evident that Mn-derived states dominate the low-energy sector, while Al-derived states dominate the high-energy sector, consistent with their respective atomic masses. A similar trend is observed in the doped compositions, including Fe/Ni-derived states that exhibit substantial hybridization in the low-energy sector due to their closely matched atomic masses. Notably, the density of states shift upwards as the atomic masses decrease, following the sequence Mn < Fe < Ni. Moreover, introducing Fe in the doped compositions leads to the lifting of phonon mode degeneracy due to the reduction in crystalline symmetry.

IV. ELECTRONIC STRUCTURE

Figure 4 shows the electronic density of states for (a) MnAl and (b) - (d) Fe/Ni substituted-MnAl obtained with spin-polarized GGA calculations. The DOS shows primarily Mn(3d) states around the Fermi level with a

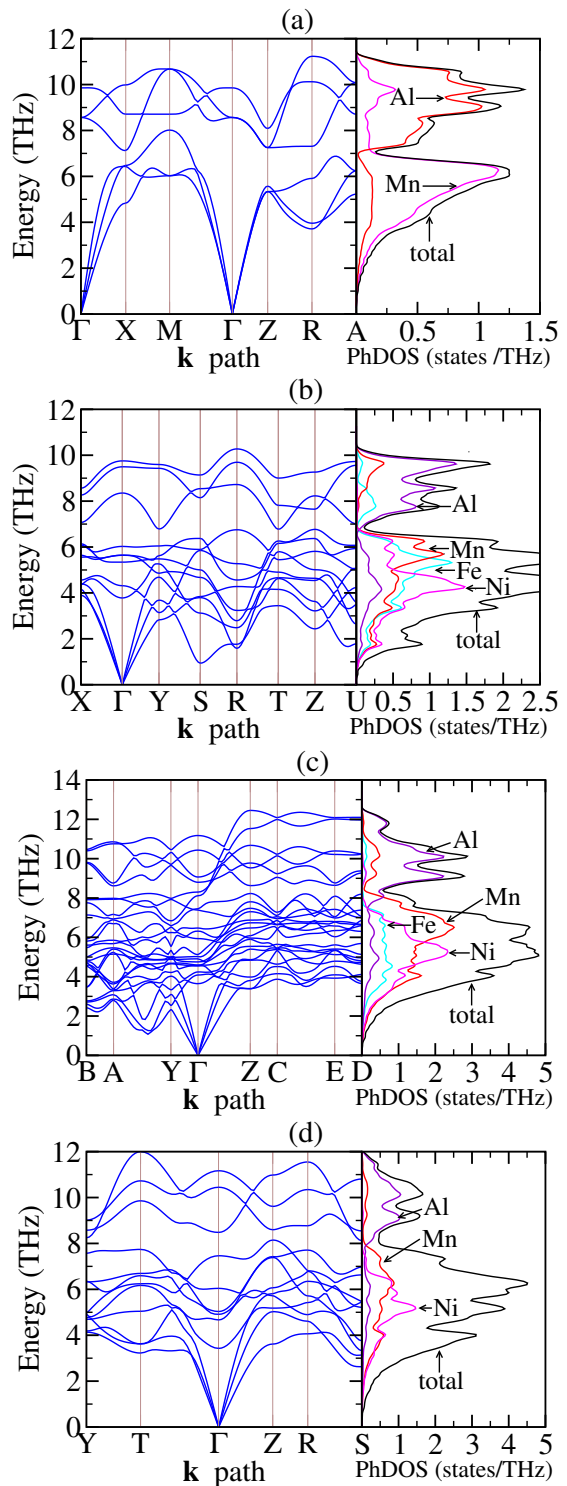


FIG. 3. Phonon band structure and density states for (a) MnAl, (b) FeMnAlNi, (c) Fe_{0.5}Mn_{1.5}AlNi, and (d) Mn₂AlNi. Total PhDOS is given per formula unit (f.u.) cell. In both cases, phonon frequencies are positive indicating their dynamical stability.

minimal admixture of Al(*sp*) states. As expected for the 3*d*-states, the spin-polarized calculations produce a magnetic state. The characteristics of the 3*d*-states around the Fermi level change with Fe/Ni substitutions. Notably, varying the Fe content brings about intriguing modifications in the electronic structure. Initially, in the absence of Fe in MnAl (Fig. 4 (a)) and Mn₂AlNi (Fig. 4 (d)), the Fermi level lies away from the peak in the DOS. This condition is closely related to a lower formation energy, as demonstrated in Fig. 2, indicating enhanced chemical stability. When the Fe content reaches 25%, a minor peak emerges in the Mn-dos (Fig. 4 (c)), which, however, remains negligible compared to the Fe and Mn-DOS peaks in Fig. 4 (b). This behavior is consistent with the observed increase in formation energy with Fe content.

The magnetic moment is susceptible to the Fe and Ni content. Substitutions affect the magnetic moment of individual magnetic atoms, thereby altering the net magnetic moment. All atoms, except Al, contribute to the magnetic moment. In the case of MnAl, each Mn atom exhibits a magnetic moment of 2.31 μ_B , which is in excellent agreement with experimental findings [4]. Effectively, the Mn spin magnetic moment increases with substitutions. For a Fe content of 25% and a Ni content of 50%, the net magnetic moment amounts to 12.53 μ_B , albeit slightly decreasing with a further increase in Fe content. It is noted that the fractional amount of doping leads to a larger supercell. For 24% Fe and 50% doping, the supercell is four times larger than the pristine MnAl unit cell, as discussed in Section II. Therefore, the magnetic moment per unit cell has to be compared accordingly. Ni is crucial in enhancing the net moment by increasing the Mn moment and contributing to the overall magnetic moment. Fe also influences the net magnetic moment similarly, although its effect is not directly proportional to the Fe content. This discrepancy may arise from differences in the crystalline electric field. Despite the presence of orbital moments for all atoms, the disparity between the hard and easy axes is significant enough to induce desirable magnetic anisotropy through spin-orbit coupling.

V. MAGNETIC ANISOTROPY

Multiple test calculations were conducted using different sets of \mathbf{k} -points. The resulting K_u values for all compounds are presented in Table IV for two converged sets of \mathbf{k} -points. It was observed that all considered compositions exhibited uniaxial anisotropy, with an easy axis aligned with the longest crystallographic direction. The value of K_u was computed as $K_u = (E_{easy} - E_{hard})/V$, where E_{easy} and E_{hard} represent the energies calculated for local spin moments along the easy and hard axes, respectively.

In the case of MnAl, the anisotropy was found to be uniaxial along the [0, 0, 1] direction, confirming that

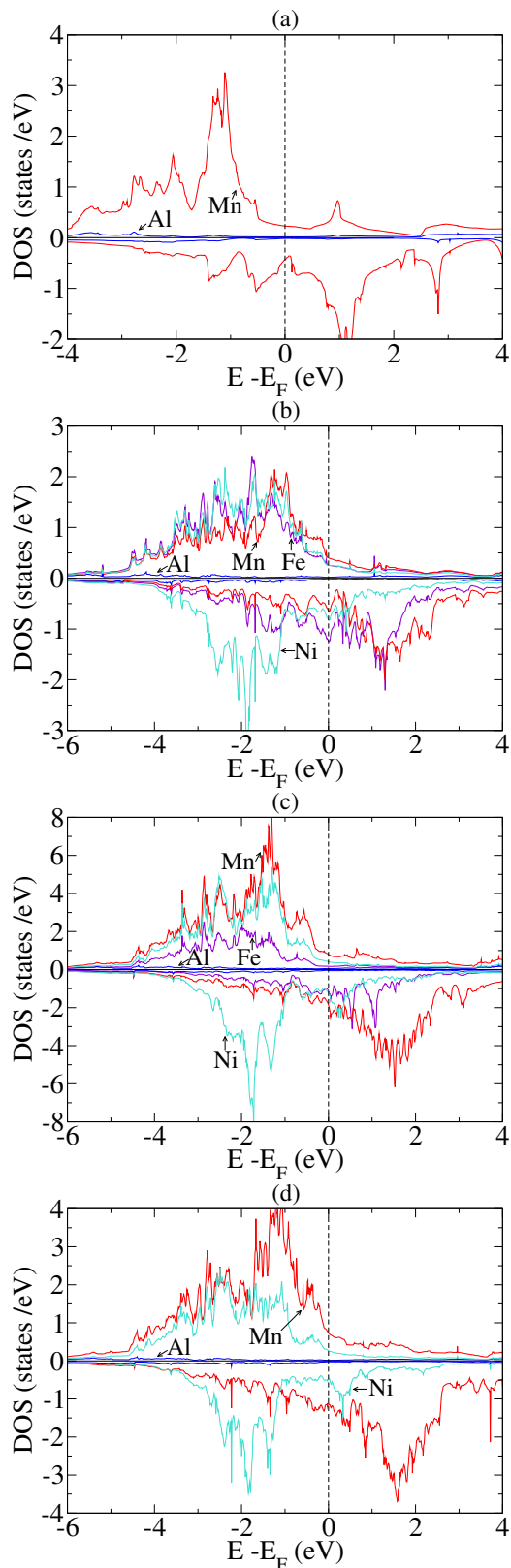


FIG. 4. Atom resolved electronic density of states (DOS) in (a) MnAl, (b) FeMnAlNi, (c) Fe_{0.5}Mn_{1.5}AlNi, and (d) Mn₂AlNi.

TABLE III. The calculated spin moment (μ_s) and orbital magnetic moment (μ_l) (obtained with dense \mathbf{k} -mesh given in Section II) and comparisons with previous theory and experimental values. The total magnetic moments are given in per unit cell. Note that the unit cell of $\text{Fe}_{0.5}\text{Mn}_{1.5}\text{AlNi}$ and Mn_2AlNi are four times, and FeMnAlNi is two times larger than MnAl . We present magnetization saturation density J_s (in T) for better comparison. The partially Fe-substituted compositions have the same crystalline symmetry, while Mn_2AlNi has a higher symmetry space group orthorhombic no. 65. For FeMnAlNi , a distorted tetragonal structure was used.

Material/moments	Fe	Mn	Al	Ni	total	J_s
MnAl						
μ_s	-	2.31	-0.04	-	2.32	1.04
μ_l	-	0.03	0.00	-	0.03	
Expt.					2.31 ^a	
Theory					2.37 ^b	
$\text{Fe}_{0.5}\text{Mn}_{1.5}\text{AlNi}$						
μ_s	2.38	3.00	-0.07	0.65	12.53	1.48
μ_l	0.08	0.02	0.00	0.06	0.25	
FeMnAlNi						
μ_s	2.04	2.96	-0.06	0.34	5.29	1.28
μ_l	0.05	0.02	0.00	0.02	0.08	
Mn_2AlNi						
μ_s		2.88	-0.07	0.6	12.65	1.46
μ_l		0.02	0.00	0.05	0.17	

TABLE IV. Comparison of calculated magnetic anisotropy constant (K_u in MJ/m^3) with experiment. For $\text{Fe}_{0.5}\text{Mn}_{1.5}\text{AlNi}$ and FeMnAlNi $[1, 0, 0]$ is easy and $[0, 1, 0]/[0, 0, 1]$ are hard axes for $\text{Fe}_{0.5}\text{Mn}_{1.5}\text{AlNi}$, while $[1, 0, 0]$ is hard and $[0, 0, 1]$ is easy axis for pristine MnAl . The values of K_u relative to the $[0, 1, 0]$ axis differ slightly depending on the choice of \mathbf{k} -points for FeMnAlNi . Mn_2AlNi is planar along $[1, 0, 0]$ and $[0, 0, 1]$ -directions.

K_u	MnAl	FeMnAlNi	$\text{Fe}_{0.5}\text{Mn}_{1.5}\text{AlNi}$	Mn_2AlNi
This work	1.53 ^a	2.34 ^b , 1.76 ^c	1.26 ^d	-0.68 ^e
	1.46 ^f	—	1.34(0.45 ^f)	-0.57
	—	—	—	—
Theory	1.5 ^g , 1.53 ^h	—	—	—
	1.67 ⁱ	—	—	—
Expt.	1.2 ^j , 1.7 ^k	—	—	—

$[1, 0, 0]$ and $[0, 1, 0]$ serve as the hard axes, while $[0, 0, 1]$ acts as the easy axis consistent with previous theoretical and experimental studies. Utilizing a \mathbf{k} -mesh size of either $9 \times 9 \times 7$ or $13 \times 13 \times 13$ yielded similar values of K_u (see Table IV), the easy axis was determined to be $[1, 0, 0]$, with $[0, 1, 0]$ and $[0, 0, 1]$ acting as the hard axes in $\text{Fe}_{0.5}\text{Mn}_{1.5}\text{AlNi}$, except for Mn_2AlNi , where the anisotropy is planar. We note that the easy axis directions are defined relative to the primitive unit cell of the alloy supercells. For instance, $[0, 0, 1]$ easy axis for MnAl corresponds to the c -axis of its unit cell, which is not

TABLE V. Magnetic anisotropy energy contributions (in meV) from different atoms in each composition. The value outside the bracket denotes the anisotropy energy contribution of the element inside the bracket. In $\text{Fe}_{0.5}\text{Mn}_{1.5}\text{AlNi}$, one Mn has negative while other remaining two have positive moments. Ni exhibits a dual nature i.e., positive or negative moments depending on the Mn doping concentration.

MnAl	FeMnAlNi	$\text{Fe}_{0.5}\text{Mn}_{1.5}\text{AlNi}^a$
0.478[Mn]	1.112[Fe]	0.446[Fe]
0.019[Al]	0.43[Mn]	-0.027, 0.140[Mn]
	0.00[Al]	-0.002[Al]
	-0.2[Ni]	0.304[Ni]

the same as the c -axis of the alloy unit cell. The size of the \mathbf{k} -mesh was adjusted proportionally to the lattice constants relative to the MnAl crystal structure.

In the case of FeMnAlNi , K_u increases by $\approx 56\%$ compared to MnAl . In the $\text{Fe}_{0.5}\text{Mn}_{1.5}\text{AlNi}$ alloy, which corresponds to a 25% Fe-doped composition, the value of K_u decreases by approximately 20%. This suggests that reducing the Fe content enhances the chemical stability, but it diminishes the value of K_u in the Ni-doped compositions. In fact, without Fe, the Mn_2AlNi compound becomes planar within the ac -plane. A more detailed understanding can be obtained through the site-resolved anisotropy, which is calculated by considering the onsite spin-orbit energy difference between the easy and hard axes for each atomic site.

According to Table V, Mn exhibits uniaxial behavior in all cases except for the 25% Fe-doped alloy, where one Mn atom becomes planar. Fe consistently exhibits uniaxial behavior and significantly contributes to K_u , consistently surpassing that of Mn. On the other hand, as expected for the sp orbital system, Al contributes the least to the magnetocrystalline anisotropy energy.

VI. MACHINE LEARNING

A. Formation energy and saturation magnetization density

Figure 5 shows a pipeline for extracting and processing crystal structure properties from the Materials Project[55]. The scraped dataset consists of 153K crystal structures with electronic and magnetic properties of magnetic and non-magnetic materials. For our purpose, we want to train only the ferromagnetic materials properties appropriate for Mn and Al binary alloy predictions. We down-select the ferromagnetic 50K materials, consisting of rare-earth and without rare-earth elements. The DFT calculated saturation magnetic density (J_s) of rare-earth-based materials in the Material project excludes the $4f$ -orbitals in the frozen- $4f$ orbital. To better predict J_s for binary alloys, we filtered out the rare-earth-based magnetic databases for ML. To be

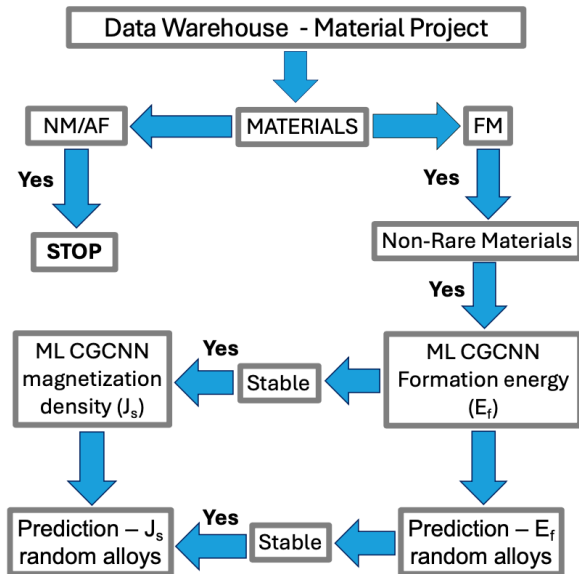


FIG. 5. Flowchart showing the ML-CGCNN workflow: Database collection, ML training on DFT parameters, and predicting new magnetic alloys compositions.

consistent, we only utilized ferromagnetic materials without rare-earth elements for ML training. In our calculations, we have 47K non-rare-earth ferromagnetic materials, which we split into 6:2:2 as training, validation, and test datasets in the crystal graph convolution neural network (CGCNN) algorithm[56]. The model has a validation accuracy the MAE of 0.098 eV/atom which is similar to that found in [56] with CGCNN and [57] obtained with the high-throughput calculations in Open Quantum Materials Database. In Figure 6, we compare E_f between the ML prediction and DFT results in the test dataset.

For J_s ML training, we used 34K non-rare-earth element-based stable compositions, including the magnetic moment in the range 1.6 - 30 μ_B per formula unit for better ML training of realistic magnetic materials. The data is split into train, validation, and test sets as a 6:3:1 ratio, which produces validation accuracy the MAE of 0.061 T. Fig. 6 shows the comparison between ML prediction and DFT results for J_s in the bottom panel.

1. Machine learning predictions on alloys

We generate random alloys by replacing Mn with Fe and Al with Ni, building a $4 \times 4 \times 4$ supercell containing 256 atoms. The total number of possible resulting compositions is 16384. The unit cell volume is scaled according to the covalent radii of the dopants to match two limits: undoped MnAl and fully-doped FeNi. The ML-predicted formation energy is shown in Fig. 7 as a function of Fe and Ni concentrations. The heatmap indicates that increasing Fe increases the stability for small

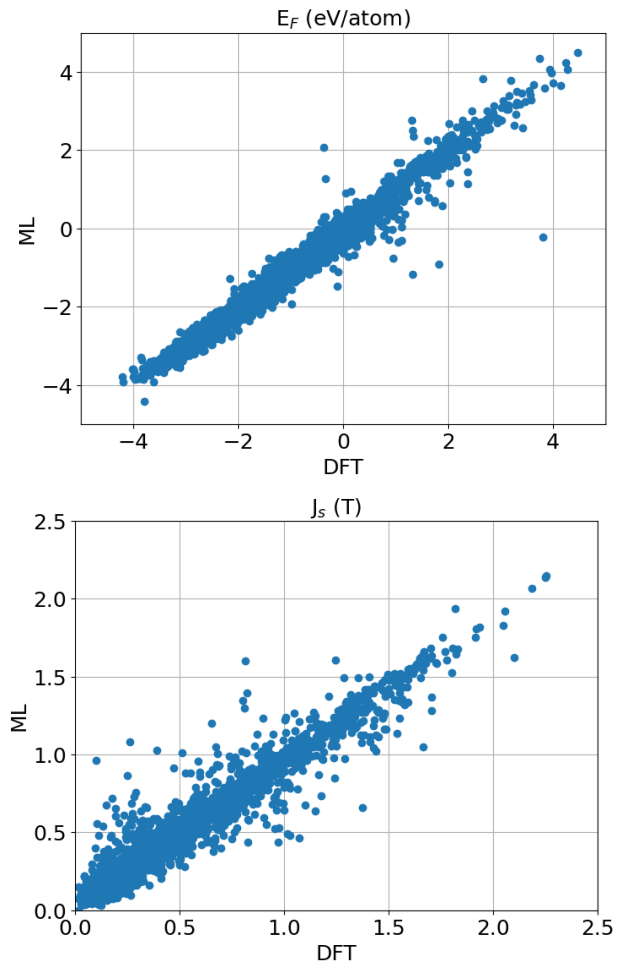


FIG. 6. Comparison of formation energies in *top* and saturation magnetization density *bottom* obtained with DFT and CGCNN-ML prediction in the test dataset.

Ni doping concentrations. While the alloy compositions are stable, the stability decreases with higher Ni-doping concentrations. The predicted formation energy of MnAl, FeAl, MnNi, and FeNi are respectively -0.28, -0.48, -0.12, and -0.08 eV/atom which are consistent with DFT values -0.27, -0.33, -0.04, and -0.07 eV/atom in Material project[55]. The predicted formation energy for 50% doped MnAl with Fe and Ni -0.28 eV/atom is slightly less than MnAl, which qualitatively agrees with our DFT calculations. The small numerical discrepancy is attributed to a mismatch in the lattice constants. The formation energy decreases with simultaneous increase in Fe and Ni concentrations.

The trend in saturation magnetization density is opposite comparing with the formation energy. Ni tends to increase it, while Fe has the opposite effect. The predicted J_s are 0.81, 0.89, 1.96, and 1.59 T for MnAl, FeAl, MnNi, and FeNi respectively. For MnFeAlNi (which amounts 50% doping) the predicted J_s is 1.17 T. The ML predictions show that Fe reduces the J_s while Ni does the opposite consistent with DFT calculations as given in

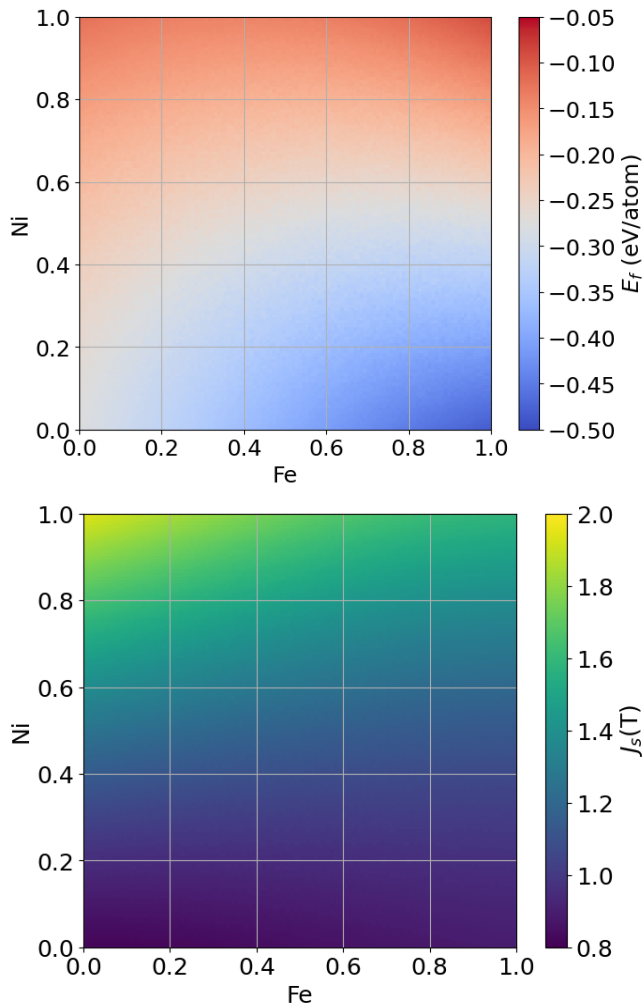


FIG. 7. Heat-map showing the variation of formation energy encoded in color map as function of dopants Fe and Ni concentrations *top* and saturation magnetization density J_s in *bottom*.

Table III.

VII. MICROMAGNETIC PREDICTION

The coercivity and hysteresis loop of the pristine and doped MnAl are investigated using micromagnetic simulations (mumax³)[58–61]. While micromagnetic analysis typically overestimates the absolute values of coercivity, it provides valuable insights into the trends and relative changes in coercivity caused by elemental substitutions[62–64].

The magnetodynamics of magnetic material is governed by the nonlinear partial differential equation for the spatio-temporal magnetization vector $\mathbf{M}(\mathbf{r}, t)$, known as the Landau–Lifshitz–Gilbert (LLG) equation [65, 66]:

TABLE VI. Magnetic parameters used in the micromagnetic simulations and predicted coercivity (H_c). A_{ex} was taken from the experiment and assumed constant. J_s and K_u were obtained from DFT calculations for each material, using the largest \mathbf{k} - mesh size.

parameters	MnAl	FeMnAlNi	Fe _{0.5} Mn _{1.5} AlNi
A_{ex} (pm)	7.6	7.6	7.6
K_u (MJ/m ³)	1.53	2.34	1.26
J_s (T)	1.04	1.28	1.48
H_c (T)	0.47	0.55	0.23

$$\frac{\partial \mathbf{M}}{\partial t} = \frac{\gamma}{1 + \alpha^2} \mathbf{M} \times \mathbf{H}_{\text{eff}} - \frac{\alpha\gamma}{1 + \alpha^2} \mathbf{M} \times \left[\mathbf{M} \times \mathbf{H}_{\text{eff}} \right], \quad (4)$$

where γ is gyromagnetic ratio, α damping constant, and \mathbf{H}_{eff} is effective magnetic field. The first term in Eq. (4) describes precession, the gyroscopic motion of the magnetic moments around the effective magnetic field, while the second damping term captures the relaxation of the moments towards equilibrium. The damping parameter α is set to 0 for time-independent scenarios, such as hysteresis loop calculations.

The effective magnetic field \mathbf{H}_{eff} consists of several contributions: the externally applied field \mathbf{H} , the demagnetizing field \mathbf{H}_{dm} arising from the long-range dipolar interactions, the exchange field \mathbf{H}_{ex} derived from the Heisenberg model, and the uniaxial anisotropy field $\mathbf{H}_{\mathbf{a}}$.

The demagnetizing field \mathbf{H}_{dm} plays a crucial role in determining the shape anisotropy of the MnAl nanostructures, which can significantly influence the coercivity and the shape of the hysteresis loop. The exchange field \mathbf{H}_{ex} , characterized by the exchange stiffness constant A_{ex} , promotes the alignment of neighboring magnetic moments and affects the domain wall width and the smoothness of the magnetization transitions.

The uniaxial anisotropy field $\mathbf{H}_{\mathbf{a}}$ is determined by the K_u and the anisotropy direction \mathbf{u} . In MnAl, the magnetocrystalline anisotropy arises from the combined effect of spin-orbit coupling of Mn *3d*-states and crystalline electric field in the ordered tetragonal L1₀ structure, leading to a strong easy-axis anisotropy along the *c*-axis.

The key material parameters K_u , M_s (J_s), and A_{ex} capture the essential physics of MnAl and enable the micromagnetic simulations of intricate magnetic structures. By systematically varying these parameters and studying their effect on the coercivity and hysteresis loop, a deeper understanding of the magnetization reversal processes and the role of material modifications in tailoring the magnetic properties of MnAl for specific applications, such as high-performance permanent magnets and magnetic recording media is gained.

As reported earlier by us in Ref. [67], micromagnetic simulation overestimates the H_c of permanent magnets by about a factor of 5 without grain boundary engineer-

ing due to Brown paradox[62, 65]. To compute a reasonable estimate of coercivity, a mesh size of 128^3 (a magnetic cuboid) was chosen with each microcell size of 1 nm^3 . The direction of the uniaxial magnetic anisotropy was taken to be uniform across grains of width 20 nm , and each grain was a random region chosen by Voronoi tessellation with the direction of the anisotropy also in a uniformly random direction. Inter-grain coupling was taken to be 10% lower across the grains than the intra-grain exchange stiffness constant, A_{ex} , value of 7.6 pm within the grains. All magnetic parameters used in the micromagnetic simulations are given in Table VI, except the inter-grain coupling and anisotropy constant, which were varied.

For the computation of the hysteresis loop, a uniform magnetic field was applied at 5 T , which was then reduced in steps of 0.01 T until -5 T was reached and the average reduced magnetization was measured (the large variation in M_s makes the reduced magnetization where the material's magnetization is put as a ratio against the total possible magnetization easier for visualization). The resulting path was smoothed with a weighted average to adjust for the relative discreteness of the mesh compared to real materials. Moreover, due to the symmetric properties of this magnetic model, the other branch of the hysteresis loop was then computed by reflection across the origin. The hysteresis loop is visualized in Fig. 8, and the coercivities of corresponding compositions are listed in Table VI.

The naïve upper limit of $2K_u/M_s = H_c$ for coercivity closely tracks the material limitations evident in the detailed micromagnetic computations despite overestimating it due to the Brown paradox [62]. However, the Brown paradox also causes the micromagnetic simulations to overestimate the actual experimental coercivity of MnAl 0.27 T , indicating that the ratios in Table VI are more important than the exact values obtained [68]. The introduction of Fe increases K_u , decreasing it slightly in $\text{Fe}_{0.5}\text{Mn}_{1.5}\text{AlNi}$. However, the additional increase in M_s due to the increase in μ_s reduces the coercivity to the lowest of the materials considered. The simple trend apparent in the table suggests increased iron content in the unit cell may further increase the K_u , leaving the M_s approximately constant, suggesting that $\text{Fe}_{1.5}\text{Mn}_{0.5}\text{AlNi}$ would have elevated H_c , requiring further material investigation.

VIII. CONCLUSION

Employing first-principles calculations and ML-CGCNN predictions, this work investigates how the substitution of Fe and Ni in the $L1_0$ type τ -phase of MnAl affects its magnetic properties. The presence of these dopants has an impact on the stability and electronic characteristics. Adding Fe yields intriguing properties dependent on the crystal structure when the Ni-content is held constant. Specifically, the formation energy de-

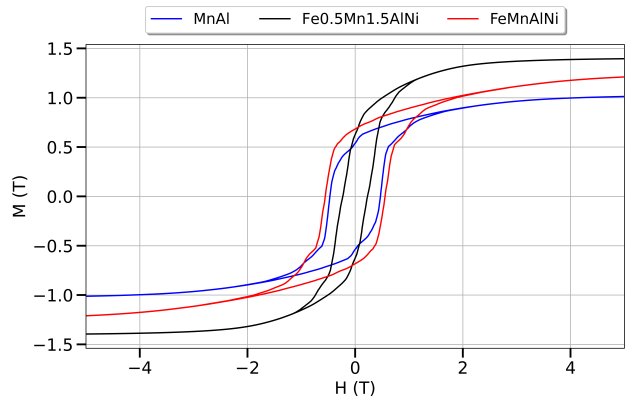


FIG. 8. The hysteresis loops of pristine and doped MnAl displaying the micromagnetically simulated normalized magnetization along the vertical axis and applied magnetic field H along the horizontal axis.

creases in distorted tetragonal and monoclinic structures, reducing Fe content. ML predictions suggest that E_f decreases with Fe for small Ni-dopings, while it increases with increasing Ni. All proposed compositions of the $L1_0$ type are mechanically and dynamically stable. Notably, a higher percentage of Fe enhances the magnetic anisotropy and magnetic moments. Surprisingly, the E_f increases reducing the stability with simultaneously Fe and Ni dopings, while the J_s increases. Remarkably, the predicted H_c is improved for the equiatomic phase obtained by simultaneous doping of Fe and Ni. Our study provides insight for stabilizing the MnAl τ $L1_0$ phase, developing H_c , and enhancing its magnetic properties by substituting Fe and Ni.

ACKNOWLEDGMENTS

This work is supported by the Critical Materials Institute, an Energy Innovation Hub funded by the U.S. Department of Energy, Office of Energy Efficiency and Renewable Energy, Advanced Manufacturing Office. The Ames National Laboratory is operated for the U.S. Department of Energy by Iowa State University of Science and Technology under Contract No. DE-AC02-07CH11358.

Appendix A: Elastic stiffness tensor

In this appendix, the calculated elastic constant tensor for all the considered MnAl alloys is presented. For

pristine MnAl it is given in (A1)

$$C_{ij} = \begin{bmatrix} 292.795 & 43.09 & 89.18 & 0.000 & 0.00 & 0.00 \\ 43.09 & 292.79 & 89.18 & 0.00 & 0.00 & 0.00 \\ 89.18 & 89.18 & 165.06 & 0.00 & 0.00 & 0.00 \\ 0.00 & 0.00 & 0.00 & 119.78 & 0.00 & 0.00 \\ 0.00 & 0.00 & 0.00 & 0.00 & 119.780 & 0.00 \\ 0.00 & 0.00 & 0.00 & 0.00 & 0.00 & 75.75 \end{bmatrix}. \quad (\text{A1})$$

It definitive positive and satisfies the criteria for mechanical stability of MnAl. The calculated elastic constant tensor for FeMnAlNi is given below A2.

$$C_{ij} = \begin{bmatrix} 207.76 & 123.64 & 105.41 & 0.00 & 0.00 & -0.39 \\ 123.64 & 290.69 & 17.15 & 0.00 & 0.00 & -5.81 \\ 105.41 & 17.15 & 236.80 & 0.00 & 0.00 & 7.61 \\ 0.00 & 0.00 & 0.00 & 28.40 & 2.33 & 0.00 \\ 0.00 & 0.00 & 0.00 & 2.33 & 115.13 & 0.00 \\ -0.39 & -5.81 & 7.61 & 0.00 & 0.00 & 92.22 \end{bmatrix}. \quad (\text{A2})$$

Similarly, for Fe_{0.5}Mn_{1.5}AlNi (A3), the elastic constant tensors are

$$C_{ij} = \begin{bmatrix} 193.55 & 114.87 & 100.31 & 0.00 & 0.00 & -2.32 \\ 114.87 & 272.15 & 24.67 & 0.00 & 0.00 & -1.66 \\ 100.31 & 24.67 & 213.36 & 0.00 & 0.00 & 1.17 \\ 0.00 & 0.00 & 0.00 & 41.58 & 0.08 & 0.00 \\ 0.00 & 0.00 & 0.00 & 0.08 & 116.72 & 0.00 \\ -2.324 & -1.66 & 1.17 & 0.00 & 0.00 & 98.71 \end{bmatrix}. \quad (\text{A3})$$

For Mn₂AlNi (A4), the diagonal elements are similar

$$C_{ij} = \begin{bmatrix} 193.15 & 111.18 & 107.63 & 0.00 & 0.00 & 0.00 \\ 111.18 & 221.44 & 15.33 & 0.00 & 0.00 & 0.00 \\ 107.63 & 15.33 & 226.37 & 0.00 & 0.00 & 0.00 \\ 0.00 & 0.00 & 0.00 & 54.44 & 0.00 & 0.00 \\ 0.00 & 0.00 & 0.00 & 0.00 & 115.64 & 0.00 \\ 0.00 & 0.00 & 0.00 & 0.00 & 0.00 & 106.71 \end{bmatrix}. \quad (\text{A4})$$

-
- [1] G. Hindricks, *Z. Anorg. Chem.* **58**, 444 (1908).
- [2] T. Ishiwara, *Sci. Rep. Tôhoku Imp. Univ.* **19**, 500 (1930).
- [3] A. J. J. Koch, P. Hokkeling, M. G. v. d. Steeg, and K. J. de Vos, New material for permanent magnets on a base of Mn and Al, *Journal of Applied Physics* **31**, S75 (1960).
- [4] H. Kôno, On the ferromagnetic phase in manganese-aluminum system, *Journal of the Physical Society of Japan* **13**, 1444 (1958).
- [5] B. Zhang and W. Soffa, The structure and properties of L1₀ ordered ferromagnets: Co-Pt, Fe-Pt, Fe-Pd and Mn-Al, *Scripta Metallurgica et Materialia* **30**, 10.1016/0956-716X(94)90182-1 (1994).
- [6] T. Klemmer, D. Hoydick, H. Okumura, B. Zhang, and W. Soffa, Magnetic hardening and coercivity mechanisms in L1₀ ordered fepd ferromagnets, *Scripta Metallurgica et Materialia* **33**, 1793 (1995), proceedings of an Acta Metallurgica Meeting on Novel Magnetic Structures and Properties.
- [7] D. P. Hoydick, E. J. Palmiere, and W. A. Soffa, Microstructural development in MnAl-base permanent magnet materials: New perspectives, *Journal of Applied Physics* **81**, 5624 (1997).
- [8] A. Sakuma, Electronic structure and magnetocrystalline anisotropy energy of MnAl, *Journal of the Physical Society of Japan* **63**, 1422 (1994), <https://doi.org/10.1143/JPSJ.63.1422>.
- [9] L. Pareti, F. Bolzoni, F. Leccabue, and A. E. Ermakov, Magnetic anisotropy of MnAl and MnAlC permanent magnet materials, *Journal of Applied Physics* **59**, 3824 (1986).
- [10] S. Zhao, T. Hozumi, P. Leclair, G. J. Mankey, and T. Suzuki, Magnetic anisotropy of τ -MnAl thin films, *IEEE Transactions on Magnetics* **51**, 1 (2015).
- [11] T. Ohtani, N. Kato, S. Kojima, K. Kojima, Y. Sakamoto, I. Konno, M. Tsukahara, and T. Kubo, Magnetic properties of Mn-Al-C permanent magnet alloys, *IEEE Transactions on Magnetics* **13**, 1328 (1977).
- [12] J. Coey, Permanent magnets: Plugging the gap, *Scripta Materialia* **67**, 524 (2012), viewpoint Set No. 51: Magnetic Materials for Energy.
- [13] C. Bhandari and D. Paudyal, Giant magnetic and optical anisotropy in cerium-substituted m-type strontium hexaferrite driven by 4f electrons, *Phys. Rev. Appl.* **20**, 024016 (2023).
- [14] C. Bhandari and D. Paudyal, Enhancing stability and magnetism of ThMn₁₂-type cerium-iron intermetallics by site substitution, *Phys. Rev. Res.* **4**, 023012 (2022).
- [15] C. Bhandari, M. E. Flatté, and D. Paudyal, Enhanced magnetic anisotropy in lanthanum m-type hexaferrites by quantum-confined charge transfer, *Phys. Rev. Mater.* **5**, 094415 (2021).
- [16] R. McCallum, L. Lewis, R. Skomski, M. Kramer, and I. Anderson, Practical aspects of modern and future permanent magnets, *Annual Review of Materials Research* **44**, 451 (2014).
- [17] J. M. D. Coey, New permanent magnets; manganese compounds, *Journal of Physics: Condensed Matter* **26**, 064211 (2014).
- [18] W. Lu, J. Niu, T. Wang, K. Xia, Z. Xiang, Y. Song, H. Zhang, S. Yoshimura, and H. Saito, Low-energy mechanically milled τ -phase MnAl alloys with high coercivity and magnetization, *Journal of Alloys and Compounds* **675**, 163 (2016).
- [19] I. Janotová, P. Švec, P. Švec, I. Mat'ko, D. Janičkovič, J. Zigo, M. Mihalkovič, J. Marcin, and I. Škorvák, Phase analysis and structure of rapidly quenched Al-Mn systems, *Journal of Alloys and Compounds* **707**, 137 (2017), selected papers presented at ISMANAM 2016, July 3rd-8th, Nara, Japan.
- [20] E. Y. Huang and M. H. Kryder, Fabrication of MnAl thin films with perpendicular anisotropy on si substrates, *Journal of Applied Physics* **117**, 17E314 (2015).
- [21] M. Oogane, K. Watanabe, H. Saruyama, M. Hosoda, P. Shahnaz, Y. Kurimoto, M. Kubota, and Y. Ando, L1₀-ordered MnAl thin films with high perpendicular mag-

- netic anisotropy, *Japanese Journal of Applied Physics* **56**, 0802A2 (2017).
- [22] L. Feng, K. Nielsch, and T. G. Woodcock, Enhanced thermal stability of the τ -phase in MnAl-C alloys with ni additions, *Journal of Alloys and Compounds* **871**, 159554 (2021).
- [23] Z. Xiang, Y. Song, B. Deng, E. Cui, L. Yu, and W. Lu, Enhanced formation and improved thermal stability of ferromagnetic τ phase in nanocrystalline Mn₅₅Al₄₅ alloys by Co addition, *Journal of Alloys and Compounds* **783**, 416 (2019).
- [24] P. L. Rossiter and M. E. Houghton, *Metals Forum* **7**, 187 (1984).
- [25] W. Dreizler and A. Menth, Transformation kinetics of the ferromagnetic alloy Mn-Al-C, *IEEE Transactions on Magnetics* **16**, 534 (1980).
- [26] M. A. Bohlmann, J. C. Koo, and J. H. Wise, Mn-Al-C for permanent magnets (invited), *Journal of Applied Physics* **52**, 2542 (1981).
- [27] R. Skomski, A. Kashyap, and J. Zhou, Atomic and micromagnetic aspects of l10 magnetism, *Scripta Materialia* **53**, 389 (2005), viewpoint set no. 36 on: L10 phases for permanent magnet and recording applications.
- [28] D. E. Laughlin, K. Srinivasan, M. Tanase, and L. Wang, Crystallographic aspects of l10 magnetic materials, *Scripta Materialia* **53**, 383 (2005), viewpoint set no. 36 on: L10 phases for permanent magnet and recording applications.
- [29] A. Edström, J. Chico, A. Jakobsson, A. Bergman, and J. Rusz, Electronic structure and magnetic properties of l10 binary alloys, *Phys. Rev. B* **90**, 014402 (2014).
- [30] P. Manchanda, A. Kashyap, J. Shield, L. Lewis, and R. Skomski, Magnetic properties of fe-doped MnAl, *Journal of Magnetism and Magnetic Materials* **365**, 88 (2014).
- [31] Q. Zeng, I. Baker, J. Cui, and Z. Yan, Structural and magnetic properties of nanostructured mnalc magnetic materials, *Journal of Magnetism and Magnetic Materials* **308**, 214 (2007).
- [32] N. Makino, Y. Kimura, and M. Suzuki, On heat treatment and magnetic properties of MnAl alloy, *Journal of the Japan Institute of Metals* **27**, 216 (1963).
- [33] J. Landuyt, G. Tendeloo, J. Broek, H. Donkersloot, and H. Zijlstra, Defect structure and magnetic properties of MnAl permanent magnet materials, *IEEE Transactions on Magnetics* **14**, 679 (1978).
- [34] F. Bittner, L. Schultz, and T. Woodcock, Twin-like defects in l10 ordered τ - MnAl-C studied by ebsd, *Acta Materialia* **101**, 48 (2015).
- [35] Y. Sakka, M. Nakamura, and K. Hoshimoto, Rapid quenching and properties of hard magnetic materials in MnAl-X (X=Ti, Cu, Ni, C, B) systems, *Journal of Materials Science* **24**, 4331 (1989).
- [36] C. Paduani, J. Schaf, A. Persiano, J. Ardisson, A. Takeuchi, and I. Riegel, Strong dependence of ferrimagnetic properties on co concentration in the Mn_{1-x}Al_{1-y}Co_{x+y} system, *Intermetallics* **18**, 1659 (2010).
- [37] S. Micán, D. Benea, R. Hirian, R. Gavrea, O. Isnard, V. Pop, and M. Coldea, Structural, electronic and magnetic properties of the Mn₅₀Al₄₆Ni₄ alloy, *Journal of Magnetism and Magnetic Materials* **401**, 841 (2016).
- [38] P. Saravanan, J.-H. Hsu, V. T. P. Vinod, M. Černík, and S. V. Kamat, Coercivity enhancement in mn-al-cu flakes produced by surfactant-assisted milling, *Applied Physics Letters* **107**, 192407 (2015).
- [39] H. X. Wang, P. Z. Si, W. Jiang, J. J. L. J. G. Lee, C. J. Choi, Q. Wu, M. Zhong, and H. L. Ge, Structural stabilizing effect of Zn substitution on MnAl and its magnetic properties, *Open Journal of Microphysics* **1**, 19 (2011).
- [40] Z. W. Liu, C. Chen, Z. G. Zheng, B. H. Tan, and R. V. Ramanujan, Phase transitions and hard magnetic properties for rapidly solidified MnAl alloys doped with c, b, and rare earth elements, *Journal of Materials Science* **47**, 2333 (2012).
- [41] J. Paier, R. Hirschl, M. Marsman, and G. Kresse, The perdew-burke-ernzerhof exchange-correlation functional applied to the G2-1 test set using a plane-wave basis set, *The Journal of Chemical Physics* **122**, 234102 (2005).
- [42] J. P. Perdew, K. Burke, and Y. Wang, Generalized gradient approximation for the exchange-correlation hole of a many-electron system, *Phys. Rev. B* **54**, 16533 (1996).
- [43] G. Kresse and J. Hafner, Ab initio molecular dynamics for liquid metals, *Phys. Rev. B* **47**, 558 (1993).
- [44] G. Kresse and D. Joubert, From ultrasoft pseudopotentials to the projector augmented-wave method, *Phys. Rev. B* **59**, 1758 (1999).
- [45] D. Hobbs, G. Kresse, and J. Hafner, Fully unconstrained noncollinear magnetism within the projector augmented-wave method, *Phys. Rev. B* **62**, 11556 (2000).
- [46] Y. Kinemuchi, A. Fujita, and K. Ozaki, High-pressure synthesis of L1₀ MnAl with near-stoichiometric composition, *Dalton Trans.* **45**, 10936 (2016).
- [47] O. Romer and E. Wachtel, Magnetische eigenschaften fester und flüssiger zink-mangan- und zink-mangan-aluminium-legierungen, *International Journal of Materials Research* **62**, 871 (1971).
- [48] F. Heusler, Über magnetische manganlegierungen, *Verh. Dtsch. Phys. Ges.* **5**, 219 (1903).
- [49] J. E. Saal, S. Kirklin, M. Aykol, B. Meredig, and C. Wolverton, Materials design and discovery with high-throughput density functional theory: The open quantum materials database (OQMD), *JOM* **65**, 1501 (2013).
- [50] F. Mouhat and F. m. c.-X. Coudert, Necessary and sufficient elastic stability conditions in various crystal systems, *Phys. Rev. B* **90**, 224104 (2014).
- [51] Z.-j. Wu, E.-j. Zhao, H.-p. Xiang, X.-f. Hao, X.-j. Liu, and J. Meng, Crystal structures and elastic properties of superhard IrN₂ and IrN₃ from first principles, *Phys. Rev. B* **76**, 054115 (2007).
- [52] C. L. Fu, A. J. Freeman, E. Wimmer, and M. Weinert, Frozen-phonon total-energy determination of structural surface phase transitions: W(001), *Phys. Rev. Lett.* **54**, 2261 (1985).
- [53] A. Togo and I. Tanaka, First principles phonon calculations in materials science, *Scr. Mater.* **108**, 1 (2015).
- [54] J. H. Park, Y. K. Hong, S. Bae, J. J. Lee, J. Jalli, G. S. Abo, N. Neveu, S. G. Kim, C. J. Choi, and J. G. Lee, Saturation magnetization and crystalline anisotropy calculations for MnAl permanent magnet, *Journal of Applied Physics* **107**, 09A731 (2010).
- [55] A. Jain, S. P. Ong, G. Hautier, W. Chen, W. D. Richards, S. Dacek, S. Cholia, D. Gunter, D. Skinner, G. Ceder, and K. A. Persson, Commentary: The Materials Project: A materials genome approach to accelerating materials innovation, *APL Materials* **1**, 011002 (2013).
- [56] T. Xie and J. C. Grossman, Crystal graph convolutional neural networks for an accurate and interpretable predic-

- tion of material properties, *Phys. Rev. Lett.* **120**, 145301 (2018).
- [57] S. Kirklin, J. E. Saal, B. Meredig, A. Thompson, J. W. Doak, M. Aykol, S. Rühl, and C. Wolverton, The open quantum materials database (OQMD): assessing the accuracy of DFT formation energies, *npj Computational Materials* **1**, 15010 (2015).
- [58] J. Leliaert, J. Mulkers, J. De Clercq, A. Coene, M. Dvornik, and B. Van Waeyenberge, Adaptively time stepping the stochastic Landau-Lifshitz-Gilbert equation at nonzero temperature: implementation and validation in MuMax³, *AIP Advances* **7**, 125010 (2017).
- [59] J. Leliaert, B. Van de Wiele, A. Vansteenkiste, L. Laurson, G. Durin, L. Dupré, and B. Van Waeyenberge, Current-driven domain wall mobility in polycrystalline permalloy nanowires: A numerical study, *Journal of Applied Physics* **115**, 233903 (2014).
- [60] L. Exl, S. Bance, F. Reichel, T. Schrefl, H. Peter Stimming, and N. J. Mauser, LaBonte’s method revisited: An effective steepest descent method for micromagnetic energy minimization, *Journal of Applied Physics* **115**, 17D118 (2014).
- [61] A. Vansteenkiste, J. Leliaert, M. Dvornik, M. Helsen, F. Garcia-Sanchez, and B. Van Waeyenberge, The design and verification of Mumax3, *AIP Advances* **4**, 107133 (2014).
- [62] W. F. Brown, Virtues and weaknesses of the domain concept, *Rev. Mod. Phys.* **17**, 15 (1945).
- [63] A. Aharoni, Theoretical search for domain nucleation, *Rev. Mod. Phys.* **34**, 227 (1962).
- [64] U. Hartmann, Origin of Brown’s coercive paradox in perfect ferromagnetic crystals, *Phys. Rev. B* **36**, 2331 (1987).
- [65] W. F. Brown, *Micromagnetics* (Interscience Publishers New York, New York, 1963).
- [66] T. Gilbert, A phenomenological theory of damping in ferromagnetic materials, *IEEE Transactions on Magnetics* **40**, 3443 (2004).
- [67] C. Bhandari, G. N. Nop, J. D. H. Smith, and D. Paudyal, Accurate machine learning predictions of coercivity in high-performance permanent magnets (2023), arXiv:2312.02475 [cond-mat.mtrl-sci].
- [68] P. Nieves, S. Arapan, J. Maudes-Raedo, R. Marticorena-Sánchez, N. Del Brío, A. Kovacs, C. Echevarria-Bonet, D. Salazar, J. Weischenberg, H. Zhang, *et al.*, Database of novel magnetic materials for high-performance permanent magnet development, *Computational materials science* **168**, 188 (2019).